Heat and mass transfer in a steady flow of Sutterby nanofluid over the surface of a stretching wedge

Usman; Lin, Ping; Ghaffari, Abuzar

Published in:
Physica Scripta

DOI:
10.1088/1402-4896/abecf7

Publication date:
2021

Document Version
Peer reviewed version

Heat and Mass Transfer in a Steady Flow of Sutterby Nanofluid over the Surface of a Stretching Wedge

Usman[1,*], Ping Lin[2,*], Abuzar Ghaffari[3]

[1]Beijing Key Laboratory for Magneto-Photoelectrical Composite and Interface Science, Department of Applied Mathematics, School of Mathematics and Physics, University of Science and Technology Beijing, Beijing 100083, China
[2]Division of Mathematics, University of Dundee, Dundee DD1 4HN, Scotland, United Kingdom
[3]Department of Mathematics, University of Education, Lahore, Attock Campus 43600, Pakistan

[*]**Corresponding author(s): Usman (usman.malik.ms@gmail.com) & Ping Lin (plin@maths.dundee.ac.uk)**

Received 18 December 2020
Revised 23 February 2021
Accepted for publication 9 March 2021
Published 30 March 2021

Abstract

The non-Newtonian Sutterby fluid model can be implied to characterize the significant characteristics of shear-thinning and shear-thickening for various ranges of the power-law index. The Sutterby fluid has a vast number of applications in engineering processes and industrial fluid mechanics. The steady two-dimensional stagnant flow of Sutterby nanofluid inside the boundary layer over a stretching wedge placed in a porous medium is investigated. The viscous incompressible fluid is electrically conducting, and a uniform magnetic field is imposed perpendicularly. The heat and mass transfer phenomenon is analyzed by incorporating the effects of nonlinear radiation, viscous dissipation, Joule heating, heat source/sink, and activation energy subject to convective-Nield boundary conditions. The physically modeled partial differential equations (PDEs) are lessened into ordinary differential equations (ODEs) with precise similarity variables. The numerical solution is obtained through the shooting method. The effects of several types of emerging parameters upon the dimensionless distributions of velocity, temperature, and concentration are exhibited graphically. A tabular comparison is presented to show the convergence and accuracy of the shooting method. It can be concluded that the pertinent parameters are altered in such a way that they have produced a substantial influence upon the dimensionless boundary layer distributions. The fluid velocity enhances, whereas temperature and concentration of nanofluid are observing two diverse behaviors for the pertinent parameters. Finally, the present study effectively fills the missing gap in the existing literature.

Keywords: Non-Newtonian Sutterby nanofluid; Stagnation point boundary layer flow, Heat, and Mass transfer; Stretching Wedge, Shooting method.

The final publication is available at IOS Press through http://dx.doi.org/10.1088/1402-4896/abecf7.

1. Introduction

Until now, the researchers have performed theoretical and experimental investigations to analyze the behavior of non-Newtonian fluids due to their numerous emerging applications in biological and industrial applications. Compared with Newtonian fluids, the non-Newtonian fluids are much appreciated because of their enormous engineering applications such as biomedical fluids, biological tissue, emulsions, food processing, paper production, and polymers lubricants, and nuclear fuel slurries. Based on the diverse rheological characteristics of non-Newtonian fluids, several rheological models have been demonstrated. Power-law fluid model, Carreau fluid model, Williamson fluid model, Sisko fluid model, Jeffery fluid model, Sutterby fluid model are some existing non-Newtonian fluid models. Among these non-Newtonian fluid models, the non-Newtonian Sutterby fluid model got much acceptance because it can be used to inspect the notable pseudo-plastic and dilatant characteristics of non-Newtonian fluids.

The Sutterby fluid model has an advantage over other flow models because it can be used to exhibit the Newtonian, shear-thinning, and shear-thickening behaviors of the fluid for various power-law index ranges. The Sutterby fluid model was firstly introduced by Sutterby [1] in 1966 and provided experimental results. He characterizes the rheological behavior of the polymer solutions with the help of viscosity data in the converging channel experiment. The Sutterby fluid model has taken a long journey to accomplish its significance [2-5]. Hayat et al. [6-7] investigated the peristaltic flow of electrically conducting Sutterby fluid inside the channel. Hayat et al. [8-9] further studied the effects of MHD and explored the three-dimensional flow of Sutterby fluid over disk geometry. Ahmad et al. [10] deliberated the flow characteristics of Sutterby fluid through dual stratification inside a squeezed channel. They adopted the Homotopy Analysis Method to tackle the governing system of nonlinear equations. Azhar et al. [11] used the shooting method to numerically investigate the stagnant flow of non-Newtonian Sutterby fluid through Cattaneo-Christov heat flux model. Khan et al. [12] analyzed the Sutterby fluid flow upon a rotatory disk with the aid of homogenous-heterogeneous reactions. Rehman et al. [13] analyzed the stagnation point flow of Sutterby fluid over a sheet, which is linearly shrinking. Imran et al. [14] theoretically explored the thermal transportation for the Sutterby fluid model, which is obeying the peristaltic mechanism with the help of chemical reactions.

The heat transfer phenomenon is extensively utilized to examine the fluid characteristics, which are naturally non-Newtonian. The heat transfer mechanism has significant importance in the manufacturing, biological and industrial processes such as water flow in reservoirs, energy storage, catalytic reactors, plasma-platelet flow in the blood, oil production in industries, heat exchangers systems, cooling of electronic devices, and power generation. Because of these promising applications, the heat transfer mechanism captured the attention of researchers, mathematicians, engineers, geologists, and architectures. Heat can be transmitted inside a body or between two bodies because of the temperature difference. Fourier's law is used to examine the heat transfer from decads. Thus, several researchers investigated the heat transfer for different fluid models over diverse geometries [15-18]. The heat transfer fluids effectively rely upon their physical features like heat density, thermal conductivity, heat capacity, and viscosity. The fluids with smaller thermal conductivity is the main problem for heat transfer. Thus, it is required to establish the mechanism through which the thermal conductivity can be enhanced. A novel way of improving thermal conductivity is by mixing the nono-sized solid particles of length 100nm within the base fluid called nanofluid. The term nanofluid was initially presented by Choi [19]. After that, Buongiorno [20] has suggested a model to examine the heat transfer

enhancement in nanofluids by investigating the seven slip phenomena such as inertia, Magnus, gravity, Brownian diffusion, diffusiophoresis, thermophoresis, and fluid drainage. He concluded that in nanofluid, thermophoresis and Brownian diffusion are the dominating slip phenomena. Azhar et al. [21] presented the numerical analysis for entropy generation upon the stagnant flow of Sutterby nanofluid upon a plate. Ahmad et al. [22] investigated the heat and mass transfer in squeezed MHD flow of Sutterby nanofluid subject to convective boundary conditions. Khan et al. [23] further considered the influence of MHD, heat source/sink, and radiative heat flux on the nonlinear mixed convective flow of Sutterby fluid between two stretchable rotatory disks and investigated the homogeneous-heterogeneous reactions. Nawaz [24] analyzed the thermal performance of hybrid nanoparticles and numerically obtained the outcomes through the finite element method. Sajid et al. [25] investigated the impact of MHD, heat source/sink, and activation energy upon the flow, heat, and mass transfer of the Maxwell-Sutterby fluid. Sohail and Naz [26] explored the MHD flow of Sutterby nanofluid within a cylinder by considering the modified models for heat and mass transfer. Rehman et al. [27] scrutinized the electrically conducting Sutterby nanofluid flow, which was flowing with the help of a linearly stretching sheet to elaborate the heat transfer phenomena. Fayyadh et al. [28] theoretically investigated the stagnation point flow and heat transfer of Sutterby nanofluid upon a permeable sheet in the presence of MHD and thermal radiation. The study of nanofluids has attracted many researchers due to its large applications in science and engineering. The researchers, under various assumptions, have performed several investigations [29-33] on nanofluids flow.

The flow and heat transfer past a wedge-shaped body is a dynamic area for the researchers from a theoretical and practical point of view due to its significant applications in engineering, chemical industry, and geographical fields, for instance, aerodynamics, heat exchangers, thermal insulation, hydrodynamics, extraction, nuclear wastes storage, groundwater pollution, and geothermal systems. Wedge flow commonly appears in supersonic flows, aircraft response to atmospheric gusts, hot and cold inclined surfaces, and engine greasing. A triangular-shaped tool, which is a portable inclined plane, and among one of the six classical simple machines, is known as a wedge. It can be utilized to separate two objects or parts of an object, hold an, or lift up an object in place. It can further be utilized to convert lateral force in the form of a transverse splitting force. The wedge flow of viscous incompressible fluid was firstly presented by Falkner and Skan [34]. They considered the static wedge, which is free of external forces, and calculated the similarity results for boundary layer flow. They concluded that the gradient of pressure plays a pivotal role in such types of flow. Hartree [35] calculated the numerical solution. The similarity variables technique reduces the boundary layer equation to ODE, which is also known as the Falkner-Skan equation. Also, this classical problem becomes the Blasius flow problem if the angle of the wedge is assumed to be zero; also, this problem diminishes to Hiemenz flow in the case when the angle of the wedge is 180°. Rajagopal et al. [36] further extended the work of Falkner and Skan in the light of second-grade fluid and obtained the solution with the perturbation method. Hamid et al. [37-38] numerically investigated the heat transfer performance upon the unsteady flow of Williamson fluid passing through the wedge. Ali et al. [39] scrutinized the heat and mass transfer of steady two-dimensional flow of Carreau fluid over a wedge with infinite shear rate viscosity effects. Goqo et al. [40] studied the entropy generation in an MHD flow of viscous nanofluid over a wedge in the light of thermal radiation. Atif et al. [41] inspected the heat and mass transfer of unsteady

two-dimensional flow of tangent hyperbolic nanofluid passing through wedge geometry. Several investigators devoted their attention to exploring the heat and mass transfer phenomenon over wedge geometry [42-48].

Motivated by the above-stated literature survey, the current research study endeavors to investigate the steady two-dimensional stagnant flow, heat, and mass transfer of the Sutterby nanofluid past a stretchable rotating wedge embedded in a porous medium. The effects of MHD, nonlinear radiation, viscous dissipation, Joule heating, heat source/sink, and activation are included in the motion, energy, and concentration equations. Flow dynamics subject to convective-Nield boundary conditions are modeled with the aid of Navier-Stokes equations, which end up in the system of mixed nonlinear differential equations through similarity transformation. Then the shooting method is employed to obtain the solution. A comprehensive parametric influence upon the dimensionless boundary layer profiles is conducted. Finally, the present study fills the missing gap in the existing literature and applicable in several different ways.

2. Sutterby Constitutive Rheological Model

Several types of fluid models satisfy various characteristics. The rheological attributes of such fluids are not completely expressed through Navier-Stokes equations. Therefore, numerous non-Newtonian fluid models have been proposed to understand the rheological attributes of complex fluids. Among these models, the non-Newtonian Sutterby fluid model has achieved its significance because it can be used effectively to demonstrate the shear-thinning and shear-thickening properties of non-Newtonian fluids for different ranges of the power-law index.

The constitutive equation for the non-Newtonian Sutterby fluid model is written as

$$\bar{\tau} = -p\bar{I} + \mu\left(\dot{\gamma}\right)\bar{A}_1, \tag{1}$$

with

$$\mu\left(\dot{\gamma}\right) = \mu\left(\frac{\mathrm{Sinh}^{-1}\left(\beta^*\dot{\gamma}\right)}{\beta^*\dot{\gamma}}\right)^n, \tag{2}$$

where $\bar{\tau}$ represents the Cauchy stress tensor, p is the pressure, $\bar{I}$ be the identity tensor, β^* be the Sutterby fluid parameter, and n denote the power-law index.

The shear rate $\dot{\gamma}$ is defined as:

$$\dot{\gamma} = \sqrt{\frac{1}{2}tr\left(\bar{A}_1^2\right)}, \tag{3}$$

The first Rivlin-Ericksen tensor $\overline{A_1}$ is given by

$$\bar{A}_1 = \nabla\bar{V} + \left(\nabla\bar{V}\right)^T, \tag{4}$$

For $\beta^*\dot{\gamma} \ll 1$, we may write

$$\mathrm{Sinh}^{-1}\left(\beta^{*}\dot{\gamma}\right)\cong\left(\beta^{*}\dot{\gamma}\right)-\frac{\left(\beta^{*}\dot{\gamma}\right)^{3}}{6}, \tag{5}$$

In the light of (5), equation (2) will become

$$\mu\left(\dot{\gamma}\right)=\mu\left(\frac{\mathrm{Sinh}^{-1}\left(\beta^{*}\dot{\gamma}\right)}{\beta^{*}\dot{\gamma}}\right)^{n}\cong\mu\left(1-\frac{\left(\beta^{*}\dot{\gamma}\right)^{2}}{6}\right)^{n}, \tag{6}$$

In the presence of (6), equation (1) will become

$$\bar{\tau}=-p\bar{I}+\mu\left(1-\frac{\left(\beta^{*}\dot{\gamma}\right)^{2}}{6}\right)^{n}\bar{A}_{1}, \tag{7}$$

The velocity (u,v), temperature T, and concentration C fields for the steady two-dimensional flow are of the following form

$$\bar{V}=\left[u\left(x,y\right),v\left(x,y\right),0\right],\ T=T\left(x,y\right),\ C=C\left(x,y\right), \tag{8}$$

where u,v denotes the components of the velocity in x and y directions.

3. Problem Formulation

Consider a steady two-dimensional stagnant flow of viscous incompressible electrically conducting Sutterby nanofluid moving upon the surface of a porous wedge, as shown in figure 1. In a particular way, the Cartesian coordinate system (x,y) is considered such that the origin, the x-axis, and the y-axis are managed at the apex, along the surface, and perpendicular to the surface of the wedge, respectively. Also, the flow is produced due to the stretching wedge through the wall velocity $u_w(x)=bx^m$ and external flow is prescribed at free stream velocity $u_e(x)=cx^m$ subject to a uniform magnetic field B_0 is imposed perpendicularly to the surface of the wedge. In which b,c,m denotes the constants such that $b>0$ and $b<0$ implies the wedge is stretching and shrinking, respectively, the power-law Falkner-Skan constant m can be written as $\beta=\frac{2m}{m+1}$ with $0\le m\le 1$ where β is the Hartree pressure gradient, and it is also written in total wedge angle Ω form as $\beta=\frac{\Omega}{\pi}$. The effects of thermal radiation, viscous dissipation, Joule heating, heat source/sink, and activation energy subject to convective-Nield boundary conditions are considered while modeling the energy and concentration equations. The Buongiorno mathematical model has been used to study and justify the nanofluid properties for thermophoresis and Brownian motion. It is further assumed that the constant temperature T_f and nano-particles concentration C_f are placed at the surface of the stretching moving wedge, and the fluid which flows away from the boundary layer is kept at uniform ambient temperature T_∞ and nano-particles concentration C_∞.

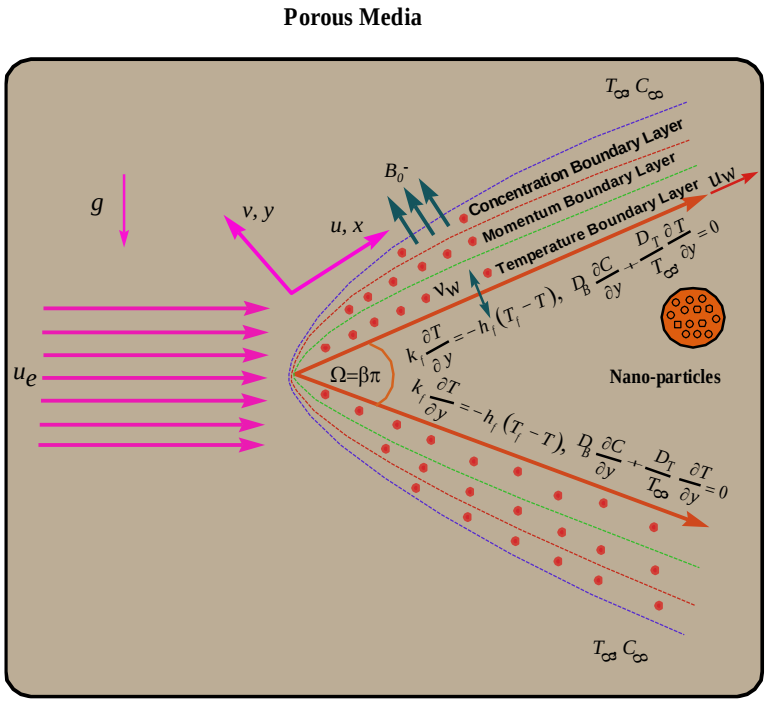

Fig. 1: The flow geometry

Thus in the light of the above-mentioned assumptions, the governing continuity, momentum, energy, and concentration equations can be written as [13]:

$$\frac{\partial u}{\partial x}+\frac{\partial v}{\partial y}=0, \tag{9}$$

$$u\frac{\partial u}{\partial x}+v\frac{\partial u}{\partial y}=u_e\frac{\partial u_e}{\partial x}+\upsilon_f\left[1-\frac{\beta^{*2}}{6}\left(\frac{\partial u}{\partial y}\right)\right]^n\left(\frac{\partial^2 u}{\partial y^2}\right)-\upsilon_f\frac{n\beta^{*2}}{6}\left[1-\frac{\beta^{*2}}{6}\left(\frac{\partial u}{\partial y}\right)\right]^{n-1}\left(\frac{\partial u}{\partial y}\right)\left(\frac{\partial^2 u}{\partial y^2}\right)$$
$$-\left(\frac{\sigma_f B_0}{\rho_f}+\frac{\upsilon_f}{k_p^*}\right)(u-u_e)+g\left[(\beta_T)_f(T-T_\infty)+(\beta_C)_f(C-C_\infty)\right]sin\left(\frac{\Omega}{2}\right), \tag{10}$$

$$u\frac{\partial T}{\partial x}+v\frac{\partial T}{\partial y}=\frac{k_f}{(\rho c_p)_f}\frac{\partial^2 T}{\partial y^2}+\frac{16\sigma^* T^3}{3(\rho c_p)_f k^*}\frac{\partial^2 T}{\partial y^2}+\frac{\mu_f}{(\rho c_p)_f}\left[1-\frac{\beta^{*2}}{6}\left(\frac{\partial u}{\partial y}\right)\right]^n\left(\frac{\partial u}{\partial y}\right)^2$$
$$-\frac{\mu_f}{(\rho c_p)_f}\frac{n\beta^{*2}}{6}\left[1-\frac{\beta^{*2}}{6}\left(\frac{\partial u}{\partial y}\right)\right]^{n-1}\left(\frac{\partial u}{\partial y}\right)\left(\frac{\partial u}{\partial y}\right)^2+\frac{\sigma_f B_0^2}{(\rho c_p)_f}u^2 \tag{11}$$
$$+\frac{Q^*}{(\rho c_p)_f}(T-T_\infty)+\tau^*\left[D_B\left(\frac{\partial T}{\partial y}\right)\left(\frac{\partial C}{\partial y}\right)+\frac{D_T}{T_\infty}\left(\frac{\partial T}{\partial y}\right)^2\right],$$

$$u\frac{\partial C}{\partial x}+v\frac{\partial C}{\partial y}=\frac{D_T}{T_\infty}\left(\frac{\partial^2 T}{\partial y^2}\right)+D_B\left(\frac{\partial^2 C}{\partial y^2}\right)-k_r^2\left(C-C_\infty\right)\left(\frac{T}{T_\infty}\right)^{n^*}exp\left(\frac{-E_a}{K^*T}\right), \tag{12}$$

The suitable boundary conditions at the surface of the wedge and away from it can be chosen as:

$$u=u_w\left(x\right)=bx^m,\ v=v_w\left(x\right)=0,\ -k_f\left(\frac{\partial T}{\partial y}\right)=h_f\left(T_f-T\right),\ D_B\left(\frac{\partial C}{\partial y}\right)+\frac{D_T}{T_\infty}\left(\frac{\partial T}{\partial y}\right)=0,\quad \text{at}\quad y=0, \tag{13}$$

$$u\to u_e\left(x\right)=cx^m,\ \ T\to T_\infty,\quad C\to C_\infty,\quad \text{when}\quad y\to\infty, \tag{14}$$

4. Similarity Transformation

The following set of similarity variables can be selected for the present problem to transform the governing scheme of differential equations (PDEs) (9-12) into ordinary differential equations (ODEs) [39]:

$$\begin{aligned}&\eta=y\sqrt{\frac{c\left(m+1\right)}{2\upsilon_f}}x^{\frac{m-1}{2}},\ \Psi\left(x,y\right)=\sqrt{\frac{2\upsilon_f c}{m+1}}x^{\frac{m+1}{2}}F\left(\eta\right),\ u=\frac{\partial\Psi}{\partial y},\ v=-\frac{\partial\Psi}{\partial x},\ \theta\left(\eta\right)=\frac{T-T_\infty}{T_f-T_\infty},\\&\varphi\left(\eta\right)=\frac{C-C_\infty}{C_f-C_\infty},\ u=cx^mF'\left(\eta\right),\ v=-\left[\sqrt{\frac{c\left(m+1\right)\upsilon_f}{2}}x^{\frac{m-1}{2}}\right]\left[F\left(\eta\right)+\left(\frac{m-1}{m+1}\right)\eta F'\left(\eta\right)\right]\end{aligned} \tag{15}$$

Thus upon using (15) into (9-12), the following system of non-dimensional coupled ODEs is obtained

$$\begin{aligned}&\left[1-\frac{\alpha}{6}\sqrt{\frac{m+1}{2}}F''\right]^nF'''-\frac{n\alpha}{6}\sqrt{\frac{m+1}{2}}\left[1-\frac{\alpha}{6}\sqrt{\frac{m+1}{2}}F''\right]^{n-1}F''F'''-\beta\left[F'^2-1\right]\\&+FF''-\frac{2}{m+1}\left[M+K_p\right]\left[F'-1\right]-\frac{2}{m+1}\left[Gr_T\theta+Gr_C\varphi\right]Sin\frac{\Omega}{2}=0,\end{aligned} \tag{16}$$

$$\begin{aligned}&\left[1+\frac{4}{3}Rd\left\{1+\left(\theta_w-1\right)\theta\right\}^3\right]\theta''+PrF\theta'+PrEc\left[1-\frac{\alpha}{6}\sqrt{\frac{m+1}{2}}F''\right]^nF''^2\\&-\frac{n\alpha}{6}\sqrt{\frac{m+1}{2}}PrEc\left[1-\frac{\alpha}{6}\sqrt{\frac{m+1}{2}}F''\right]^{n-1}F''^3+\frac{2}{m+1}PrEcMF'^2\\&+\frac{2}{m+1}PrQ\theta+Pr\left[N_b\theta'\varphi'+N_t\theta'^2\right]=0,\end{aligned} \tag{17}$$

$$\varphi''+\frac{N_t}{N_b}\theta''+LePrF\varphi'-\frac{2}{m+1}K_rPrLe\varphi\left(1+\delta\theta\right)^{n^*}exp\left(\frac{-E}{1+\delta\theta}\right)=0, \tag{18}$$

The transformed boundary conditions (13-14) can be transmuted as

$$F\left(\eta\right)=0,\ F'\left(\eta\right)=\lambda,\ \theta'\left(\eta\right)=-Bi\left(1-\theta\left(\eta\right)\right),\ N_b\varphi'\left(\eta\right)+N_t\theta'\left(\eta\right)=0,\quad \text{at}\quad y=0, \tag{19}$$

$$F'\left(\eta\right)=1,\ \theta\left(\eta\right)=0,\ \varphi\left(\eta\right)=0,\quad \text{when}\quad y\to\infty, \tag{20}$$

where the dimensionless parameters are as follows

$$\beta=\frac{2m}{m+1},\ \alpha=\beta^{*2}\sqrt{\frac{c^3x^{3m-1}}{\upsilon_f}},\ M=\frac{\sigma_f B_0^2}{c\rho_f},\ K_p=\frac{\upsilon_f}{k_p^*},\ Gr_T=\frac{g\left(\beta_T\right)_f\left(T_f-T_\infty\right)}{c^2x^{2m-1}},$$
$$Gr_C=\frac{g\left(\beta_C\right)_f\left(C_f-C_\infty\right)}{c^2x^{2m-1}},\ \lambda=\frac{b}{c},\ Rd=\frac{-4\sigma^*T_\infty^3}{k_fk^*},\ \ \theta_w=\frac{T_f}{T_\infty},\ Q=\frac{Q^*}{c\left(\rho c_p\right)_f},$$
$$Pr=\frac{\upsilon_f}{\alpha_f},\ Ec=\frac{c^2x^{2m}}{\left(c_p\right)_f\left(T_f-T_\infty\right)},\ N_t=\frac{\tau^*D_T\left(T_f-T_\infty\right)}{T_\infty\upsilon_f},\ N_b=\frac{\tau^*D_B\left(C_f-C_\infty\right)}{\upsilon_f},$$
$$K_r=\frac{k_r^2}{c},\ \delta=\frac{T_f-T_\infty}{T_\infty},\ Le=\frac{\upsilon_f}{D_B},\ E=\frac{E_a}{K^*T_\infty},\ Bi=\frac{-h_f}{T_f}\sqrt{\frac{2\upsilon_f}{c\left(m+1\right)x^{m-1}}},\tag{21}$$

5. Physical Quantities

5.1. Skin Friction

The skin friction coefficient or surface drag force or gradient of the velocity C_{Fx} is given by

$$C_{Fx}=\frac{\tau_w}{\rho_f u_e^2},\tag{22}$$

The shear stress τ_w is defined as

$$\tau_w=\mu_f\left[\left\{1-\frac{\beta^{*2}}{6}\left(\frac{\partial u}{\partial y}\right)\right\}^n\left(\frac{\partial u}{\partial y}\right)\right]_{y=0},\tag{23}$$

The non-dimensional form is

$$\sqrt{Re_x}C_{Fx}=\sqrt{\frac{m+1}{2}}\left[\left\{1-\frac{\alpha}{6}\sqrt{\frac{m+1}{2}}F''\left(\eta\right)\right\}^n F''\left(\eta\right)\right]_{\eta=0},\tag{24}$$

5.2. Local Nusselt Number

The local Nusselt number or heat transfer rate, or gradient of temperature Nu_x is defined as

$$Nu_x=\frac{xq_w}{k_f\left(T_f-T_\infty\right)},\tag{25}$$

Here the wall heat flux q_w can be written as

$$q_w=\left[-k_f\frac{\partial T}{\partial y}+\left(q_x\right)_w\right]_{y=0},\tag{26}$$

The dimensionless form is

$$\frac{Nu_x}{\sqrt{Re_x}} = -\sqrt{\frac{m+1}{2}}\left[\left\{1+Rd\left(1+\left(\theta_w-1\right)\theta\left(\eta\right)\right)^3\right\}\theta'\left(\eta\right)\right]_{\eta=0}, \tag{27}$$

5.3. Local Sherwood Number

The local Sherwood number or mass transfer rate or gradient of concentration Sh_x is delineated as

$$Sh_x = \frac{xq_m}{D_B\left(C_f - C_\infty\right)}, \tag{28}$$

The wall mass flux q_m is written as

$$q_m = -D_B\left[\frac{\partial C}{\partial y}\right]_{y=0}, \tag{29}$$

The dimensionless will take the form

$$\frac{Sh_x}{\sqrt{Re_x}} = -\sqrt{\frac{m+1}{2}}\left[\varphi'\left(\eta\right)\right]_{\eta=0}, \tag{30}$$

Where $Re_x = \frac{cx^{m+1}}{\nu_f}$ denotes the local Reynolds number.

6. Shooting Method

The shooting method is helpful in solving the PDEs (16-18) subject to boundary conditions (19-20) because of its low computational cost and high level of accuracy. Therefore the solution methodology of the shooting method is based on the following steps:

Step I: The boundary value problem (BVP) can be transmuted into an initial value problem (IVP) by defining the derivatives as follows:

$$F = y_1,\ F' = y_2,\ F'' = y_3,\ \theta = y_4,\ \theta' = y_5,\ \varphi = y_6,\ \varphi' = y_7, \tag{31}$$

This assumption will lead to the reduction of the ODEs (16-18) into the system of 7 first-order mixed equations in the form of 7 functions as:

$$y_1' = y_2, \tag{32}$$

$$y_2' = y_3, \tag{33}$$

$$y_3' = \frac{\beta\left[y_2^2-1\right] - y_1y_3 + \left(\frac{2}{m+1}\right)\left[M+K_p\right]\left[y_2-1\right] + \left(\frac{2}{m+1}\right)\left[Gr_T y_4 + Gr_C y_6\right]Sin\left(\frac{\Omega}{2}\right)}{\left[1-\frac{\alpha}{6}\sqrt{\frac{m+1}{2}}y_3\right]^{n-1}\left[1-\left(n+1\right)\frac{\alpha}{6}\sqrt{\frac{m+1}{2}}y_3\right]}, \tag{34}$$

$$y_4' = y_5, \tag{35}$$

$$y_5' = \frac{\left[\begin{array}{c} -Pry_1y_5 - PrEc\left[1-\frac{\alpha}{6}\sqrt{\frac{m+1}{2}}y_3\right]^n y_3^2 + \frac{n\alpha}{6}\sqrt{\frac{m+1}{2}}PrEc\left[1-\frac{\alpha}{6}\sqrt{\frac{m+1}{2}}y_3\right]^{n-1} y_3^3 \\ -\left(\frac{2}{m+1}\right)PrEcMy_2^2 - \left(\frac{2}{m+1}\right)PrQy_4 - Pr\left[N_b y_5 y_7 + N_t y_5^2\right] \end{array}\right]}{\left[1+\frac{4}{3}Rd\left\{1+\left(\theta_w-1\right)y_4\right\}^3\right]}, \tag{36}$$

$$y_6' = y_7, \tag{37}$$

$$y_7' = -\left(\frac{N_t}{N_b}\right)y_5' - LePry_1y_7 + \left(\frac{2}{m+1}\right)K_r PrLey_6\left(1+\delta y_4\right)^{n^*} exp\left(\frac{-E}{1+\delta y_4}\right), \tag{38}$$

The boundary conditions are

$$y_1(\eta)=0,\ y_2(\eta)=\lambda,\ y_5(\eta)=Bi\left(1-y_4(\eta)\right),\ N_b y_7(\eta)+N_t y_5(\eta)=0, \quad \text{at} \quad y=0, \tag{39}$$

$$y_2(\eta)=1,\ y_4(\eta)=0,\ y_6(\eta)=0, \quad \text{when} \quad y\to\infty, \tag{40}$$

Step II: The initial conditions which are missing can be calculated by numerically integrating the differential equations at boundary value as an IVP.

Step III: By estimating the dependent variable at the boundary point, the precision of the calculated missing initial conditions can be assured. If the calculated value of the missing initial is not converging, then another appropriate value can be guessed. This method can be repeated until the desired degree of accuracy is accomplished between the initial conditions, which are given and computed.

Step IV: The RK method can, therefore, be used to obtain the solution of the first-order IVP coupled system along with the initial conditions which are missing and calculated.

7. Convergence Analysis

The shooting method is employed to tackle the PDEs (16-18) with boundary conditions (19-20) in Matlab software. A comparison in a limiting case is established in table 1 for the calculated numerical values of $-F''(0)$ with the previously existing outcomes from the literature. It is witnessed that the outcomes are converging, and a remarkable agreement is examined. It means that the shooting method is supremely effective for such type of complex fluid flow problems because of its low computational cost and high accuracy level.

Table 1: Comparison of $-F''(0)$ for diverse β when $\alpha = m = M = K_p = Gr_T = Gr_C = \Omega = \lambda = 0$ and $n = 1$.

β	$-F''(0)$				
	Present Study	**Ref. [36]**	**Ref. [37]**	**Ref. [42]**	**Ref. [46]**
0.00	0.469600	-	0.469601	0.469600	0.4696
0.05	0.531130	0.531130	-	0.531350	-
0.10	0.587035	0.587035	0.587036	0.587139	0.5869
0.20	0.686708	0.686708	-	0.686141	-
0.30	0.774755	0.774755	0.774754	0.775524	0.7747

0.40	0.854421	0.854421	-	0.854937	-
0.50	0.927680	0.927680	0.927680	0.927905	0.8543
0.60	0.995836	0.995836	-	0.995757	-
0.70	1.059807	-		1.059421	-
0.80	1.120268	1.120268	-	1.119574	-
0.90	1.177728	-		1.176730	-
1.00	1.232585	1.232585	1.232588	1.231289	-
1.20	1.335722	1.335722	-	1.333833	-
1.60	1.521514	1.521514	-	1.518488	-
2.00	1.687217	-		1.683095	-

8. Results and Discussion

In the present study, the focus was to investigate the influence of MHD, nonlinear radiation, viscous dissipation, Joule heating, heat source/sink, and activation upon the steady two-dimensional stagnant flow and heat, as well as the mass transfer of viscous incompressible electrically conducting Sutterby nanofluid over the surface of stretching moving wedge subject to convective-Nield boundary conditions. The influence of several-class of pertinent parameters like the Hartee pressure gradient parameter β, Sutterby fluid parameter α, magnetic parameter M, permeability parameter K_p, temperature Grashof number Gr_T, concentration Grashof number Gr_C, the Falkner-Skan power-law constant m, radiation parameter Rd, surface heating parameter θ_w, heat source/sink parameter Q, Prandtl number Pr, Eckert number Ec, thermophoresis parameter N_t, Brownian motion parameter N_b, the constant chemical reaction rate parameter K_r, temperature difference parameter δ, Lewis number Le, activation energy parameter E, and Biot number Bi on the non-dimensional boundary layer distributions of velocity $F'(\eta)$, temperature $\theta(\eta)$, and concentration $\varphi(\eta)$ are analyzed. Figures 2-15 are plotted upon scaling the parameters as $N = 2.0, \beta = 0.2, \alpha = 0.1, M = 1.0,\ K_p = 0.4,\ Gr_T = Gr_C = 0.6,\ m = 0.3,\ \lambda = 0.5,\ Rd = 1.0, \theta_w = 1.5, Q = 0.2, Pr = 6.8, Ec = 0.6, N_t = 0.25, N_b = 0.35, K_r = 0.8,\ \Omega = 120,\ n^* = 0.5, \delta = 0.6, Le = 1.2, E = 1.5, Bi = 0.2.$

8.1. Velocity Profiles

Figures 2-4 are plotted to show the upshots of the magnetic parameter M, permeability parameter K_p, Sutterby fluid parameter α, Hartee pressure gradient parameter β, temperature Grashof number Gr_T, concentration Grashof number Gr_C upon fluid velocity $F'(\eta)$ alongside non-dimensional similarity variable η.

The effects of magnetic parameter M and permeability parameter K_p upon the dimensionless distribution of fluid velocity $F'(\eta)$ are depicted in figure 2. The profile of $F'(\eta)$ is attained its minimum value when $M = 0$, but when $M \neq 0$, it is observed increasing along η. Whenever the magnetic field is applied perpendicularly, it introduces the Lorentz force in an electrically conducting fluid, which creates resistance within the motion of liquid particles, due to which the momentum boundary layer drags back to the surface. The thickness of the velocity boundary layer decreases for the flow over the moving wedge. The Lorentz force is physically produced under electric and magnetic fields, which diminishes the thickness of the momentum boundary layer by opposing the transport phenomenon. It is further observed that the rise in the permeability parameter K_p the fluid velocity augments. Physically, it can be expressed as the parameter K_p boosts, the regime turned out to be more porous, and the magnitude of the Darcian force diminishes, which slows down the motion of the fluid particles. Thus it decreases the resistance as K_p increases

because of which flow gradually encounters the lesser amount of drag and decreases the flow retardation thereby. Therefore, the permeability parameter increases the motion of the fluid inside the boundary layer.

Also, the increment in the fluid velocity is slightly larger for M than from K_p.

The upshots of the Sutterby fluid parameter α and Hartee pressure gradient parameter β (or wedge angle parameter) upon the non-dimensional fluid velocity profile $F'(\eta)$ are deliberated in figure 3. The profile $F'(\eta)$ is escalating along η for increasing values of the parameters α and β. The mathematical expression of the non-Newtonian Sutterby nanofluid parameter tells us that when the parameter α increases, the kinematic viscosity decreases, which results in additional fluid deformation, and consequently, fluid velocity escalates. Also, $\beta = 0$ refers to the zero degrees wedge angle, which means the flat plate, and for $\beta = 1/2$ states to the wedge angle 90 degrees, which implies the vertical plate. The fluid velocity increases and becomes steeper for rising values of the parameter β. The parameter β denotes the pressure gradient measure; that is why the positivity of β refers to the favorable or negative pressure gradient. In the accelerated flow case (or for positive values of β), the velocity distribution squeezes nearer and nearer to the wall surface, which does not allow the backflow or overshoot phenomenon to occur.

Figure 4 deals to explore the effects of the temperature and concentration Grashof numbers (Gr_T, Gr_C) upon the non-dimensional distribution of the $F'(\eta)$. It is found that for the higher estimation of both the parameters, the fluid velocity increases along η. The increase in the parameter Gr_T causes the existence of the thermal force, which assists the flow because of which fluid velocity enhances, and it leads to diminishing the thickness of the thermal boundary layer. The increase in the Gr_C lead to the occurrence of thermal and solutal buoyancy, which can enhance the fluid velocity. The thickness of the boundary layer is thinner for the parameter Gr_T from the parameter Gr_C.

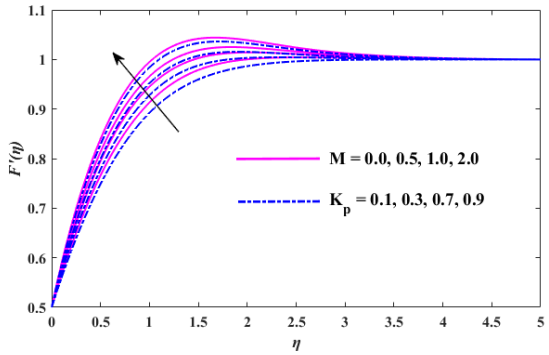

Fig. 2: Upshots of M and K_p upon $F'(\eta)$.

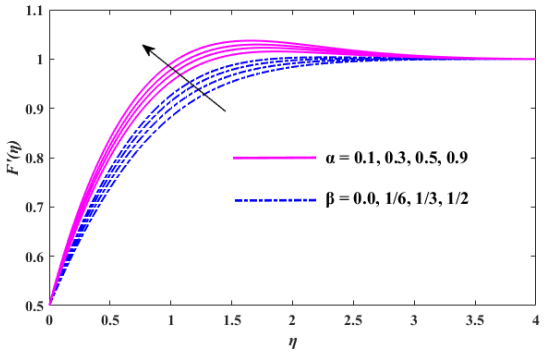

Fig. 3: Upshots of α and β upon $F'(\eta)$.

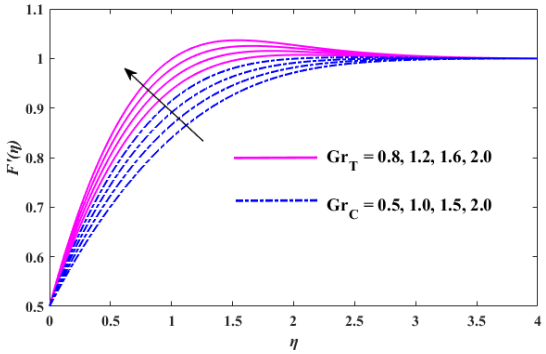

Fig. 4: Upshots of Gr_T and Gr_C upon $F'(\eta)$.

8.2. Temperature Profiles

Figures 5-10 displays the upshots of the surface heating parameter θ_w, radiation parameter Rd, the Hartee pressure gradient parameter β, Sutterby fluid parameter α, magnetic parameter M, the Falkner-Skan power-law constant m, thermophoresis parameter N_t , Brownian motion parameter N_b , heat source/sink parameter Q , and Biot number Bi upon the dimensionless distribution of temperature $\theta(\eta)$ along dimensionless similarity variable η.

The effects of the parameters θ_w and Rd upon $\theta(\eta)$ are portrayed in figure 5. The temperature is escalating along η for rising both the parameters. It is stated that $\theta_w = 1.0$ corresponds to the linear radiation and $\theta_w > 1.0$ means the nonlinear radiation. The parameter θ_w elucidates the comparison of the temperature between larger to ambient walls. When θ_w escalates the fluid temperatures become very large from ambient temperature, which increases the thermal state of the temperature. The escalation in the temperature is more considerable for nonlinear radiation than from linear radiation. Also, the temperature increases from 0 to higher estimation of the parameter Rd. The physical concept is that the rise in the parameter Rd leads to a decreasing mean absorption coefficient, which produces additional heat towards the fluid direction, which causes the escalation of the temperature inside the boundary layer. The boundary layer thickness increases as both parameter increases.

Figure 6 depicts the influence of the parameters α and β upon the profile of $\theta(\eta)$. It is examined that the temperature is decaying along η for growing values of both parameters. The rise in the parameter α causes decrements in the fluid temperature and thickness boundary layer. Further, the temperature decays for rising the parameter β. The maximum temperature is noticed for the fluid flow upon the flat plate, i.e., $\beta = 0$, whereas the minimum temperature is detected for the vertical plate, i.e., $\beta \neq 0$. Thus, the pressure gradient becomes zero, and the temperature is enhanced due to the fluid motion at the wedge surface. The boundary layer thickness reduces when both parameters increases, and this reduction is more extensive for β.

Figure 7 displays the effects of the parameters M and m upon the dimensionless distribution $\theta(\eta)$ of temperature. It is observed that the profile $\theta(\eta)$ is predicting two diverse behaviors along η for increasing values of both the parameters (M, m). The temperature is escalating for the parameter M whereas decaying for the parameter m. The magnetic parameter M portrays the Joule heating effects on the temperature profile. The temperature is minimum when $M = 0$, and increases when $M \neq 0$. The concept behind this is that the increase in the magnetic parameter causes the existence of Lorentz force, which generates friction upon the flow, and this friction produces more heat energy, which ultimately enhances the temperature profile within the flow. On the other hand, the temperature decreases as the parameter m increases. The thickness of the boundary layer turned thicker for increasing M while it becomes thinner for increasing m.

The upshots of the parameters N_t (solid lines) and N_b (dashed lines) on the profile $\theta(\eta)$ are captured in figure 8. The increasing profile of the temperature along η is examined for increasing N_t and N_b. The increases in N_b causes the rise in the thermal conductivity of the base fluid and surge in N_t lead to the thermophoretic force production because of the temperature gradient, which keeps the rapid flow away from the wedge. Thus the hot fluid is dragged away from the surface of the wedge, and that is why the thermal boundary layer turns thicker. The thickness of the boundary layer is marginally higher for the thermophoresis parameter N_t than from the Brownian motion parameter N_b.

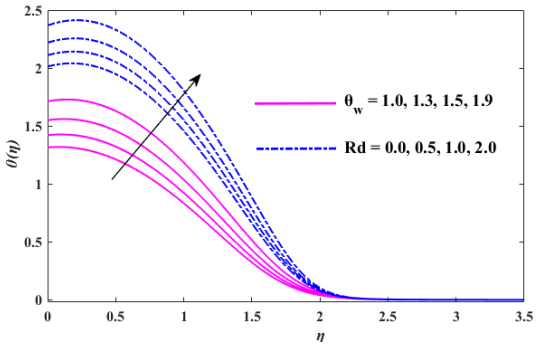

Fig. 5: Upshots of θ_w and Rd upon $\theta(\eta)$.

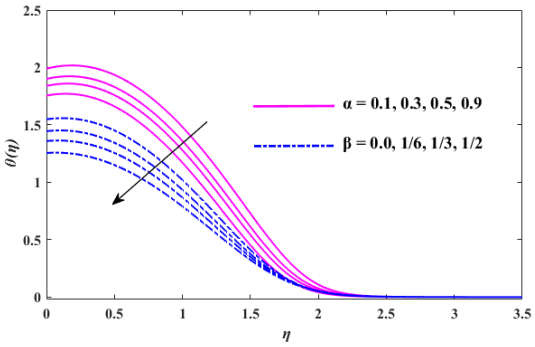

Fig. 6: Upshots of α and β upon $\theta(\eta)$.

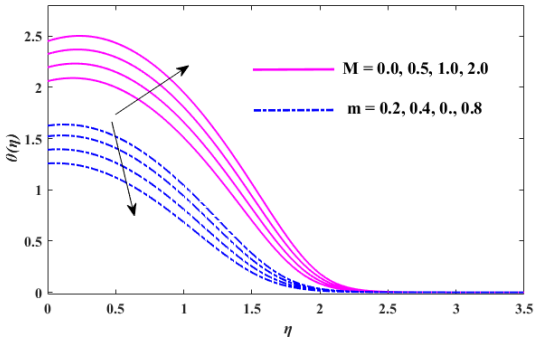

Fig. 7: Upshots of M and m upon $\theta(\eta)$.

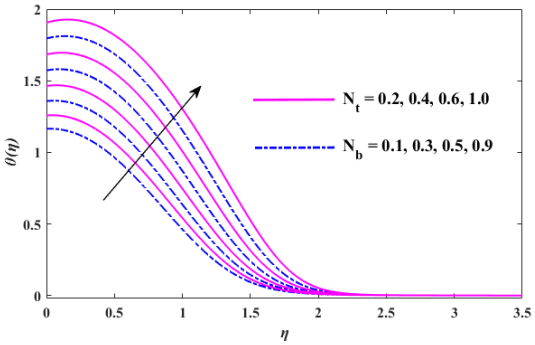

Fig. 8: Upshots of N_t and N_b upon $\theta(\eta)$.

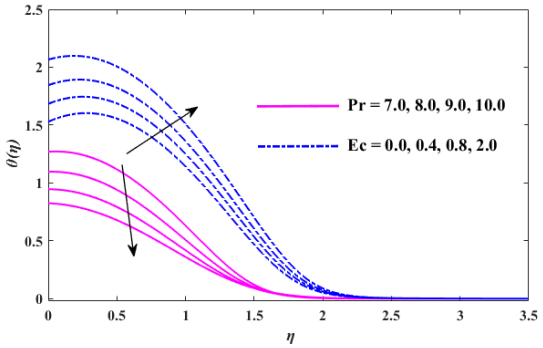

Fig. 9: Upshots of Pr and Ec upon $\theta(\eta)$.

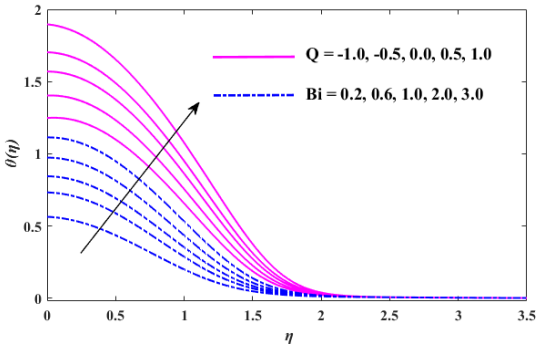

Fig. 10: Upshots of Q and Bi upon $\theta(\eta)$.

The influence of the parameters Pr and Ec upon the profile of temperature $\theta(\eta)$ are exhibited in figure 9. It is implied that the temperature distribution is observing two different trends, i.e., escalating for the parameter Ec but decaying for the parameter Pr. Mainly the Prandtl number is connected with thermal and momentum diffusivities. When Pr rises, the thermal diffusivity becomes weaker, which leads to the domination of momentum diffusivity over thermal diffusivity, and consequently, temperature decays inside the boundary layer. The temperature is escalating for increasing the parameter Ec. The Eckert number Ec presents the influence of viscous dissipation. The rise in the parameter Ec causes a conversion of kinetic energy into heat energy, which enhances the fluid thermal conductivity, and as a result, temperature escalates. Prandtl number helps control the thickness of the boundary layer, whereas the thickness of the boundary layer escalates for the Eckert number.

Figure 10 displays the variation within the temperature profile $\theta(\eta)$ because of the parameters Q and Bi. The temperature is augmenting along η for both parameters. For $Q < 0$ leads to the internal heat sink, which acts as a heat absorber, and for $Q > 0$ indicates the internal heat source, which behaves as a heat generator. In the internal heat sink process, temperature decreases because of energy absorption. During the internal heat source process, a large quantity of heat is generated, which increases the temperature. The Biot number Bi means the ratio of heat transfer resistance within the body to body surface resistance. When $Bi > 0.1$, the heat convection at the surface becomes faster from heat conduction, and temperature gradients are considerable. Further, the Biot number is precisely associated with the coefficient of heat transfer. When the numerical value of Bi progresses, the fluid conductivity decreases but enhances the heat transfer coefficient, which causes a rise in the fluid temperature. The thickness of the boundary layer decays with the enhancement in both the parameters.

8.3. Concentration Profiles

The effects of the parameter like thermophoresis parameter N_t, Brownian motion parameter N_b, Prandtl number Pr, Lewis number Le, the constant chemical reaction rate parameter K_r, the Falkner-Skan power-law constant m, activation energy parameter E, and temperature difference parameter δ upon the non-dimensional distribution of the concentration $\varphi(\eta)$ along dimensionless similarity, variable η are deliberated in figures 11-14.

Figure 11 elucidates the impacts of the parameters N_t and N_b upon $\varphi(\eta)$. The profile of $\varphi(\eta)$ examines two trends along η for various values of the thermophoresis and Brownian motion parameters (N_b, N_t). The concentration of nanoparticles enhances as the thermophoresis parameter increases. Because during the thermophoresis process, nanoparticles are dispersed from the warm surface to ambient fluid as the nano-sized particles undergo resistance from the heated surface. In this way, the thermophoretic force permits nanoparticles to transfer the heat from the surface towards the moving fluid. The thickness of the concentration boundary layer turns thicker. The concentration of nanoparticles decays as the Brownian motion parameter increases. It can be physically explained as the Brownian motion happens because of the nano-particles collision with that of base fluid inside a nanofluid system. The heat conduction is demonstrated by Brownian diffusion. The nanoparticles enlarge the area of the wedge surface for heat transfer. A nanofluid is mainly a two-phase system in which the arbitrary motion of the nanoparticles increases the kinetic energy. Nevertheless, the diffusion of nanoparticles is strongly affected by Brownian motion. The thickness of the concentration boundary layer declines in the case of Brownian motion.

The impressions of the parameters Pr and Le upon $\varphi(\eta)$ are accentuated in figure 12. The nanoparticle concentration and the concentration boundary layer thickness decays along η for the higher approximation of Pr and Le. The rise in the Prandtl number owns a weaker thermal diffusivity, which reduces the temperature and concentration of the nanoparticles. Also, the concentration of nanoparticles reduces as Lewis number Le enhances. The Lewis number expresses the ratio between mass and momentum diffusivities. During mass and momentum diffusion convection, the Lewis number is used to characterize the fluid flow. It is further connected with the relative thickness of the mass transfer boundary layer and hydrodynamic layer. The rise in the parameter Le lead to the occurrence of substantial molecular motions that reduces the Brownian diffusion coefficient D_B because the Lewis number is in an inverse

relationship with D_B due to which particles diffuse inside the fluid deeper. Therefore, the decrease in the diffusivity implies the declination in the concentration of nanoparticles.

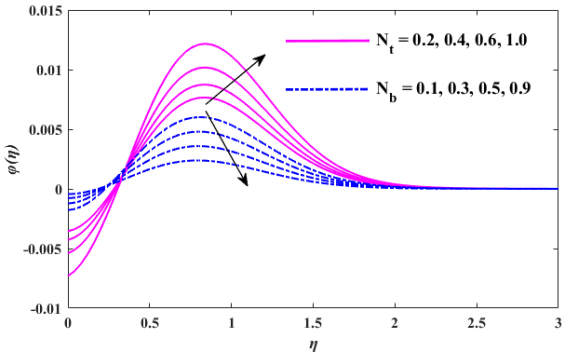

Fig. 11: Upshots of N_t and N_b upon $\varphi(\eta)$.

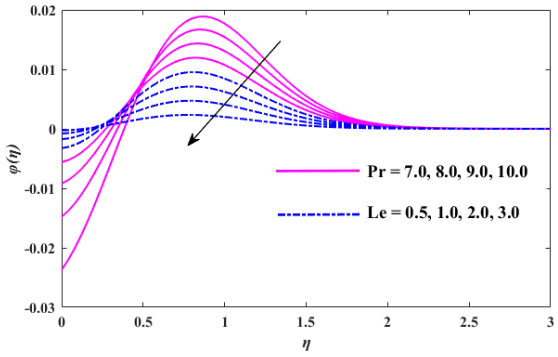

Fig. 12: Upshots of Pr and Le upon $\varphi(\eta)$.

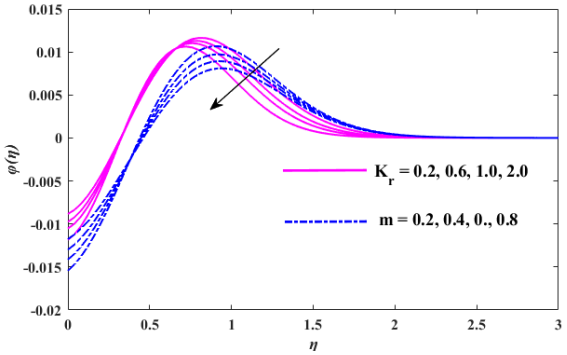

Fig. 13: Upshots of K_r and m upon $\varphi(\eta)$.

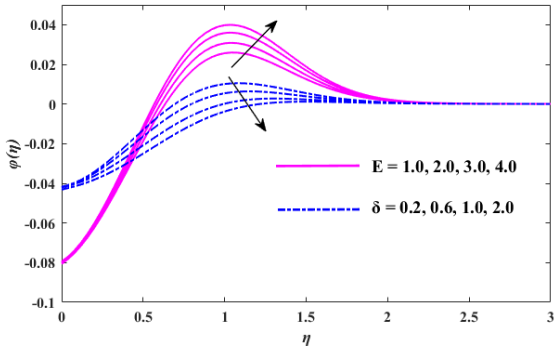

Fig. 14: Upshots of E and δ upon $\varphi(\eta)$.

Figure 13 interprets the effects of the parameters K_r and m upon the non-dimensional profile of $\varphi(\eta)$. The concentration of nanoparticles and the thickness of the concentration boundary layer decays along η for different parameters' values. Whenever the chemical reaction parameter K_r enhances the number of solute molecules experiencing the chemical reaction gets escalated because of which the concentration of nanoparticles reduces. Thus the thickness of the solutal boundary layer is greatly decreased by a destructive chemical reaction rate. Further, the concentration decreases as the Falkner-Skan power-law constant m rises. The thickness of the concentration boundary layer is thicker near the wall for the parameter K_r and thinner for the parameter m, whereas away from the wall, this behavior gets reversed.

The upshots of the parameters E and δ upon the dimensionless profile $\varphi(\eta)$ are encapsulated in figure 14. Two different types of trends are observed along η for rising values of the activation energy parameter E, and temperature difference parameter δ. The lowest form of energy is required to begin a reaction, which is referred to as activation energy. It is shown that a decrease in the reaction rate constant is brought about at lower temperatures and high activation energy, which gradually decelerates the chemical reaction, and an increase in the mass fraction field occurs. Therefore the concentration of nanoparticles is escalating as Arrhenius activation energy parameter E increases. Also, the escalation in the temperature difference parameter δ causes the increment in the destructive rate of chemical reaction because of which the concentration of nanoparticles reduces. The thickness of the concentration boundary layer is thicker for the parameter E, whereas it is thinner for the parameter δ.

8.4. Skin Friction Coefficient

Table 2 elucidates the numerical assessment of the skin friction coefficient $\sqrt{Re_x}C_{Fx}$ in the case when $n = 1.0$, and $n = 2.0$ for diverse values of the parameters $\alpha, m, \beta, M, K_p, Gr_T, Gr_C$ and λ. The other parameters are set as $Rd = 1.0,\ \theta_w = 1.5,\ Q = 0.2,\ Pr = 6.8,\ Ec = 0.6,\ N_t = 0.25,\ N_b = 0.35,\ K_r = 0.8, \Omega = 120, n^* = 0.5, \delta = 0.6, Le = 1.2, E = 1.5, Bi = 0.2$. It is observed that the skin friction reduces with the increase of the Sutterby fluid parameter, whereas it increases with the increase of the Hartee pressure gradient parameter. The magnetic field also enhances the skin friction at the wedge surface; this enhancement is due to field lines in the fluid perpendicular to the fluid motion. These magnetic field lines resist the fluid from flowing, and fluid particles stick with magnetic field lines. It is also seen that temperature Grashof enhances the skin friction and concentration Grashof reduces the skin friction.

Table 2: Calculated values of the skin friction coefficient.

α	m	β	M	K_p	Gr_T	Gr_C	λ	$\sqrt{Re_x}C_{Fx}$	
								$n = 1.0$	$n = 2.0$
0.1	0.3	1/4	0.5	0.3	0.6	0.6	0.5	0.7398	0.7359
0.3								0.7320	0.7202
0.5								0.7239	0.7040
0.9								0.7072	0.6692
0.1	0.4							0.7504	0.7453
	0.6							0.7691	0.7547
	0.8							0.7892	0.7744
	0.3	1/6						0.7444	0.7306
		1/3						0.7611	0.7571
		1/2						0.7972	0.7831
		1/4	0.0					0.5874	0.5744
			1.0					0.7878	0.7739
			2.0					0.9054	0.8904
			0.5	0.5				0.7820	0.7784
				0.7				0.8132	0.8095
				0.9				0.8435	0.8396
				0.3	1.0			0.8604	0.8569
					1.5			0.8837	0.8702
					2.0			0.9072	0.8936
					0.6	1.0		0.7286	0.7152
						1.5		0.7070	0.6937
						2.0		0.6826	0.6795
						0.6	0.0	1.2310	1.2181
							0.3	0.8990	0.8825
							0.6	0.5367	0.5246
							1.0	0.0218	0.0118

8.5. Local Nusselt Number

The values of the local Nusselt number $\frac{Nu_x}{\sqrt{Re_x}}$ alongside the different values of the parameters $\alpha, Rd, \theta_w, Pr, m, Ec, M, Q, N_t, N_b$ and Bi in the case when $n = 1.0$, and $n = 2.0$ are computed in Table 3. The remaining parameters are scaled as $\beta = 0.2, K_p = 0.4, Gr_T = Gr_C = 0.6,\ \lambda = 0.5, K_r = 0.8, \Omega = 120, n^* = 0.5, \delta = 0.6, Le = 1.2, E = 1.5$. It is seen from the tabulated data of the Nusselt number that the heat transfer rate at

the wedge surface falls with the enhancement of the radiation effects. Similar effects were captured with the Sutterby fluid parameter variation, whereas the Eckert and magnetic parameters enhanced the heat transfer rate at the wedge surface. The heat transfer rate is decreased with an increase in thermophoresis effects, whereas it increases with the increase of Brownian motion of the nanoparticles.

Table 3: Calculated values of local Nusselt number.

α	Rd	θ_w	Pr	m	Ec	M	Q	N_t	N_b	Bi	$\frac{Nu_x}{\sqrt{Re_x}}$	
											$n = 1.0$	$n = 2.0$
0.1	0.5	1.3	7.0	0.3	0.5	0.5	0.5	0.2	0.1	0.2	0.3879	0.3845
0.3											0.3809	0.3706
0.5											0.3737	0.3560
0.9											0.3584	0.3244
0.1	1.0										0.3408	0.3362
	1.5										0.3019	0.2979
	2.0										0.2679	0.2545
	0.5	1.0									0.4334	0.4264
		1.5									0.3659	0.3505
		1.9									0.3031	0.2986
		1.3	8.0								0.4236	0.4114
			9.0								0.5529	0.5450
			10.0								0.6463	0.6324
			7.0	0.4							0.3116	0.3094
				0.6							0.2623	0.2503
				0.8							0.1884	0.1665
				0.3	1.0						0.4972	0.4840
					1.5						0.6056	0.5907
					2.0						0.9008	0.8942
					0.5	0.0					0.5610	0.5497
						1.0					0.7538	0.7327
						2.0					0.9408	0.9299
						0.5	-1.0				0.1244	0.1146
							0.0				0.2909	0.2804
							1.0				0.5128	0.5013
							0.5	0.4			0.3487	0.3337
								0.6			0.2649	0.2506
								1.0			0.1420	0.1376
								0.2	0.3		0.4322	0.4205
									0.5		0.5240	0.5323
									0.9		0.6490	0.6374
									0.1	0.6	0.4173	0.4040
										1.0	0.5222	0.5179
										2.0	0.6280	0.6127
										3.0	0.7307	0.7248

8.6. Local Sherwood Number

Table 4 demonstrates the calculated values of the local Sherwood number $\frac{Sh_x}{\sqrt{Re_x}}$ for the different values of the parameters $N_t, N_b, Le, Pr, m, K_r, \delta$, and E in the case when $n = 1.0$, and $n = 2.0$. The other involved parameters are adjusted as $\beta = 0.2, \alpha = 0.1, M = 1.0, K_p = 0.4, Gr_T = Gr_C = 0.6, \lambda = 0.5, Rd = 1.0, \theta_w = 1.5, Q = 0.2, Ec = 0.6, \Omega = 120, n^* = 0.5, Bi = 0.2$. It is examined from the tabulated data of the local Sherwood number that the mass

transfer rate enhances with the enhancement in the thermophoresis parameter, Brownian motion parameter, Lewis number, Prandtl number. Similar effects are noticed for the constant chemical reaction rate parameter and activation energy parameter. Whereas the mass transfer rate decreases as a positive constant increases. The escalation in mass transfer rate for $n = 1.0$ is slightly larger than from $n = 2$.

Table 4: Calculated values of the local Sherwood number.

N_t	N_b	Le	Pr	m	K_r	δ	E	$\frac{Sh_x}{\sqrt{Re_x}}$	
								$n = 1.0$	$n = 2.0$
0.2	0.1	0.5	7.0	0.3	0.2	0.2	1.0	0.3379	0.3263
0.4								0.5419	0.5299
0.6								0.6824	0.6701
1.0								0.8648	0.8521
0.2	0.3							0.4012	0.3908
	0.5							0.5293	0.5192
	0.9							0.7247	0.7194
	0.1	1.0						0.3824	0.3707
		2.0						0.4496	0.4376
		3.0						0.5474	0.5350
		0.5	8.0					0.3990	0.3871
			9.0					0.4722	0.4600
			10.0					0.5475	0.5349
			7.0	0.4				0.3192	0.3075
				0.6				0.2949	0.2831
				0.8				0.2737	0.2617
				0.3	0.6			0.3627	0.3511
					1.0			0.3966	0.3850
					2.0			0.4469	0.4353
					0.2	0.6		0.3593	0.3477
						1.0		0.3796	0.3681
						2.0		0.4004	0.3989
						0.2	2.0	0.3774	0.3659
							3.0	0.4071	0.3956
							4.0	0.4470	0.4355
							5.0	0.5069	0.4954

8.7. Stream Lines

In figure 15, the streamlines are plotted to predict the flow behavior for the various m. The variation of m are assumed 0.1, 0.3, 0.4, 1.0. It can be seen that for $m = 0.1$ and $m = 0.3$ the one-sided flow occurs near the stagnation point. Whereas for $m = 0.4$ and higher values, the flow occurs on both sides of the stagnated line.

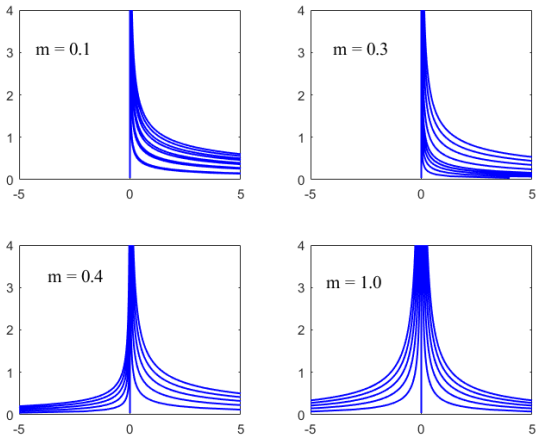

Fig. 15: Streamlines patterns for m.

8.8. Conclusion

A new mathematical model is developed to investigate the influence of MHD, nonlinear radiation, viscous dissipation, Joule heating, heat source/sink, and activation energy subject to convective-Nield boundary conditions upon a steady two-dimensional stagnant flow of electrically conducting viscous incompressible Sutterby nanofluid upon a surface of stretching wedge embedded in a porous medium. The shooting method is used to obtain the results numerically to demonstrate the characteristics of boundary layer flow as well as heat and mass transfer through their dependence on several types of pertinent parameters. Therefore, the following conclusion can be drawn from the present study:

- The fluid velocity is effectively enhanced through the appropriate change of the parameters $M, K_p, \alpha, \beta, Gr_T$ and Gr_C.
- The fluid temperature is observed increasing with the parameter M, whereas decreasing with the parameters m, α, and β.
- An escalation in the nanofluid temperature is noticed with the parameters $Rd, \theta_w, N_t, N_b, Ec$, and Q but it decays through the parameter Ec.
- The nanofluid temperature is effectively enhanced through the utilization of convective-Nield's boundary conditions.
- The concentration of nanoparticles is increased by the proper alterations in the parameters N_t, and E.
- The change in the parameters N_b, Pr, Le, K_r, m, and δ slowed down the nanoparticle concentration.

Acknowledgments

This work is partially supported by the National Natural Science Foundation of China (Nos. 11771040 and 11861131004) and the Fundamental Research Funds for the Central Universities (No. 06500073).

Declaration of competing interest

The authors affirm that they have no known competing financial interests or personal relationships that could have appeared to influence the scientific work reported in this paper.

Nomenclature

		Dimensions			Dimensions
x, y	Cartesian coordinates	**[L]**	F	Dimensionless velocity	-
u, v	Horizontal and vertical velocity components	**[L/T]**	Gr_T	Temperature Grashof number	-
u_e	Free stream velocity	**[L/T]**	Gr_C	Concentration Grashof number	-
u_w	Stretching velocity	**[L/T]**	R_d	Radiation parameter	-
n	Power-law index	-	Pr	Prandtl number	-
B_0	Uniform magnetic field	**[$M^{½}L^{½}T^{-2}$]**	Ec	Eckert number	-
k_p^*	Permeability parameter of the porous medium	**[L^2]**	Q	Dimensionless heat source/sink parameter	-
g	Acceleration due to gravity	**[L/T^2]**	N_b	Brownian motion parameter	-
T	Temperature	**[K]**	N_t	Thermophoresis parameter	-
T_f	Wall temperature	**[K]**	K_r	The constant chemical reaction rate parameter	-
T_∞	Ambient temperature	**[K]**	Bi	Biot number	-
C	Concentration	-	Nu_x	Local Nusselt number	-
C_f	Wall concentration	-	Sh_x	Local Sherwood number	-
C_∞	Ambient concentration	-	q_m	Wall mass flux	-
k_f	Thermal conductivity	**[$MLT^{-3}K^{-1}$]**	**Greek symbols**		
$(c_p)_f$	Specific heat capacity of the base fluid	**[$L^2T^{-2}K^{-1}$]**	β^*	Sutterby fluid coefficient	-
p	Pressure	**[M L^{-1} T^{-2}]**	$\bar{\tau}$	Cauchy stress tensor	**[M L^{-1} T^{-2}]**
$\bar{V}$	Velocity vector	**[L T^{-1}]**	$\dot{\gamma}$	Shear rate	**[T^{-1}]**
I	Identity tensor	-	υ_f	Effective kinematic viscosity	-
Q^*	Heat source/sink coefficient	**[M L^2T^{-1}]**	μ_f	Effective dynamic viscosity	-
D_B	Coefficient of Brownian diffusion	-	σ_f	Effective electrical conductivity	-
D_T	Coefficient Thermophoresis diffusion	-	ρ_f	Effective fluid density	**[M L^{-3}]**
k_r	The constant chemical reaction rate	-	$(\beta_T)_f$	Thermal expansion coefficient	-
n^*	Fitted constant rate	-	$(\beta_C)_f$	Volumetric expansion coefficient	-
E_a	Activation energy	-	Ω	Total wedge angle	-
K^*	Boltzmann constant	-	τ^*	The ratio of the heat capacity	-
m	Positive constant	-	η	Non-dimensional similarity variable	-
h_f	Heat transfer coefficient	-	ψ	Stream function	-

c	Constant rate	-	θ	Non-dimensional temperature	-
M	Magnetic parameter	-	φ	Non-dimensional concentration	-
K_p	Dimensionless permeability parameter	-	α	Sutterby fluid parameter	-
Le	Lewis number	-	β	Hartee pressure gradient parameter	-
E	Activation energy parameter	-	θ_w	Surface heating parameter	**[K]**
C_{Fx}	Skin friction coefficient	-	δ	Temperature difference parameter	**[K]**
Re_x	Local Reynolds number	-	λ	Velocity ratio parameter	-
q_w	Wall heat flux	-	τ_w	Shear stress	**[M L^{-1} T^{-2}]**

References

[1] Sutterby J L 1966 Laminar converging flow of dilute polymer solutions in conical sections: Part I. Viscosity data, new viscosity model, tube flow solution. AIChE Journal, **12(1)** 63–68. doi:10.1002/aic.690120114.

[2] Tetsu F, Osamu M, Motoo F, Hiroshi T and Kentaro M 1973 Natural convective heat transfer from a vertical isothermal surface to a non-Newtonian Sutterby fluid, International Journal of Heat and Mass Transfer, **16(12)** 2177–2187. doi:10.1016/0017-9310(73)90005-7.

[3] Batra R L and Eissa M 1994 Laminar forced convection heat transfer of a sutterby model fluid in an eccentric annulus, Mechanics Research Communications, **21(2)** 147–152. doi:10.1016/0093-6413(94)90087-6.

[4] Akbar N S 2015 Biomathematical study of Sutterby fluid model for blood flow in stenosed arteries, International Journal of Biomathematics, **08(06)** 1550075. doi:10.1142/s1793524515500758.

[5] Hayat T, Ahmad S, Khan M I and Alsaedi A 2018 Modeling Chemically Reactive Flow of Sutterby Nanofluid by a Rotating Disk in Presence of Heat Generation/Absorption. Communications in Theoretical Physics, **69(5)** 569. doi:10.1088/0253-6102/69/5/569.

[6] Hayat T, Zahir H, Mustafa M and Alsaedi A 2016 Peristaltic flow of Sutterby fluid in a vertical channel with radiative heat transfer and compliant walls: A numerical study. Results in Physics, **6**, 805–810. doi:10.1016/j.rinp.2016.10.015.

[7] Hayat T, Quratulain, Alsaadi F, Rafiq M and Ahmad B 2017 On effects of thermal radiation and radial magnetic field for peristalsis of sutterby liquid in a curved channel with wall properties, Chinese Journal of Physics, **55(5)** 2005–2024. doi:10.1016/j.cjph.2017.08.004.

[8] Hayat T, Afzal S, Khan M I and Alsaedi A 2019 Irreversibility aspects to flow of Sutterby fluid subject to nonlinear heat flux and Joule heating, Applied Nanoscience, **9**,1215–1226. doi:10.1007/s13204-019-01015-3.

[9] Hayat T, Masood F, Qayyum S and Alsaedi A 2019 Sutterby fluid flow subject to homogeneous-heterogeneous reactions and nonlinear radiation. Physica A: Statistical Mechanics and Its Applications, **544**, 123439 doi:10.1016/j.physa.2019.123439.

[10] Ahmad S, Farooq M, Javed M and Anjum A. (2018). Double stratification effects in chemically reactive squeezed Sutterby fluid flow with thermal radiation and mixed convection. Results in Physics, **8**, 1250–1259. doi:10.1016/j.rinp.2018.01.043.

[11] Azhar E, Iqbal Z, Ijaz S, and Maraj E N 2018 Numerical approach for stagnation point flow of Sutterby fluid impinging to Cattaneo–Christov heat flux model. Pramana, **91(5)** 61. doi:10.1007/s12043-018-1640-z.

[12] Khan M I, Qayyum S, Hayat T and Alsaedi A 2019 Stratified flow of Sutterby fluid with homogeneous-heterogeneous reactions and Cattaneo-Christov heat flux, International Journal of Numerical Methods for Heat & Fluid Flow, **29(8)** 2977-2992, doi: 10.1108/HFF-12-2018-0762.

[13] Rehman S, Mir N A, Alqarni M S, Farooq M, Malik M Y 2019 Analysis of heat generation/absorption in thermally stratified Sutterby fluid flow with Cattaneo–Christov theory, Microsystem Technologies, **25,** 3365–3373 https://doi.org/10.1007/s00542-019-04522-z.

[14] Imran N, Javed M, Sohail M, Thounthong P and Abdelmalek Z 2020 Theoretical exploration of thermal transportation with chemical reactions for sutterby fluid model obeying peristaltic mechanism, Journal of Materials Research and Technology, **9(4)** 7449–7459. doi:10.1016/j.jmrt.2020.04.071.

[15] Noreen S, Kausar T, Tripathi D, Ain Q U and Lu D 2020 Heat transfer analysis on creeping flow Carreau fluid driven by peristaltic pumping in an inclined asymmetric channel, Thermal Science and Engineering Progress, **17** 100486, 100486. doi:10.1016/j.tsep.2020.100486.

[16] Usman, Lin P and Ghaffari A 2020 Steady flow and heat transfer of the power-law fluid between two stretchable rotating disks with non-uniform heat source/sink. Journal of Thermal Analysis and Calorimetry, doi:10.1007/s10973-020-10142-x.

[17] Kumar R, Sood S, Shehzad S A and Sheikholeslami M 2017 Radiative heat transfer study for flow of non-Newtonian nanofluid past a Riga plate with variable thickness. Journal of Molecular Liquids, **248** 143–152. doi:10.1016/j.molliq.2017.10.018.

[18] Yang W, Chen X, Zhang X, Zheng L and Liu F 2019 Flow and heat transfer of double fractional Maxwell fluids over a stretching sheet with variable thickness. Applied Mathematical Modelling, **80** 204-216, doi:10.1016/j.apm.2019.11.017.

[19] Choi S U S 1995 Enhancing thermal conductivity of fluids with nanoparticles, Proc. Int. Mech. Eng. Congress. San Francisco, USA, ASME, FED 231/MD **66** 1 99–105.

[20] J. Buongiorno 2006 Convective Transport in Nanofluids," ASME Journal of Heat Transfer, 128(3) 240-250 pp. 240-250. http://dx.doi.org/10.1115/1.2150834.

[21] Azhar E, Iqbal Z and Maraj E N 2016 Impact of Entropy Generation on Stagnation-Point Flow of Sutterby Nanofluid: A Numerical Analysis. Zeitschrift Für Naturforschung A, **71(9)** doi:10.1515/zna-2016-0188.

[22] Ahmad S, Farooq M, Anjum A and Sheriff S 2019 Investigation of Convective Heat and Mass Conditions in Squeeze Flow of a Hydro-magnetic Sutterby Fluid, Journal of Magnetics **24(4)** 688-697.

[23] Khan M I, Khan M W A, Ahmad S, Hayat T, Alsaedi A 2019 Transportation of homogeneous-heterogeneous reactions in flow of Sutterby fluid confined between two co-axially rotating disks Phys. Scr. https://doi.org/10.1088/1402-4896/ab4627.

[24] Nawaz M. 2019 Role of hybrid nanoparticles in thermal performance of Sutterby fluid, the ethylene glycol. Physica A: Statistical Mechanics and Its Applications **537** 122447. doi:10.1016/j.physa.2019.122447.

[25] Sajid T, Tanveer S, Sabir Z and Guirao J L G 2020 Impact of Activation Energy and Temperature-Dependent Heat Source/Sink on Maxwell–Sutterby Fluid. Mathematical Problems in Engineering, **2020** 1–15. doi:10.1155/2020/5251804.

[26] Sohail M and Naz R 2020 Modified heat and mass transmission models in the magnetohydrodynamic flow of Sutterby nanofluid in stretching cylinder. Physica A: Statistical Mechanics and Its Applications, **549** 124088. doi:10.1016/j.physa.2019.124088.

[27] Rehman S, Mir A N, Farooq M, Rizwan M, Ahmad F, Ahmad S and Ahmad B 2019 Analysis of thermally stratified flow of Sutterby nanofluid with zero mass flux condition. Journal of Materials Research and Technology 9(2) 1631-1639, doi:10.1016/j.jmrt.2019.11.088.

[28] Fayyadh M M, Naganthran K, Basir M F M, Hashim I and Roslan R. 2020 Radiative MHD Sutterby Nanofluid Flow Past a Moving Sheet: Scaling Group Analysis. Mathematics, **8(9)** 1430, doi:10.3390/math8091430.

[29] Bilal M and Ramzan M 2019 Hall current effect on unsteady rotational flow of carbon nanotubes with dust particles and nonlinear thermal radiation in Darcy–Forchheimer porous media. Journal of Thermal Analysis and Calorimetry, **138(5)**, 3127-3137.

[30] Kumar K G, Hani E H B, Assad M E H, Rahimi-Gorji M and Nadeem S 2021 A novel approach for investigation of heat transfer enhancement with ferromagnetic hybrid nanofluid by considering solar radiation. Microsystem Technologies, **27(1)** 97-104.

[31] Bilal M and Urva Y 2020 Analysis of non-Newtonian fluid flow over fine rotating thin needle for variable viscosity and activation energy, Archive of Applied Mechanics **85** 1-17.

[32] Iqbal M S, Mustafa I, Riaz I, Ghaffari A and Khan W A 2021 Influence of carbon nanotubes on heat transfer in MHD nanofluid flow over a stretchable rotating disk: A numerical study, Heat Transfer, **50(1)**, 619-637.

[33] Iqbal M S, Malik F, Mustafa I, Ghaffari A, Riaz A and Nisar K S 2020 Impact of induced magnetic field on thermal enhancement in gravity driven Fe3O4 ferrofluid flow through vertical non-isothermal surface. Results in Physics, 19, 103472.

[34] Falkner V M and Skan S W 1931 Solutions of the boundary layer equations. Philosophical Magazine, **7** 865-896.

[35] D R Hartree 1937 On an equation occurring in Falkner and Skan's approximate treatment of the equations of the boundary layer Proc. Camb. Phil. Soc. **33**, 223–239.

[36] R. Rajagopal AS, Gupta and T Y Na 1983 A note on the Falkner-Skan flows of a non-Newtonian fluid, Int. J. Non-Linear Mech., **18** 313-320.

[37] Hamid A, Hashim, Khan M 2018 Numerical investigation on heat transfer performance in time dependent flow of Williamson fluid past a wedge-shaped geometry, Results in Phys. **9** 479e485, https://doi.org/10.1016/j.rinp.2018.01.025.

[38] Hashim, Khan M and Hamid A. (2018). Numerical investigation on time-dependent flow of Williamson nanofluid along with heat and mass transfer characteristics past a wedge geometry. International Journal of Heat and Mass Transfer, **118** 480–491. doi:10.1016/j.ijheatmasstransfer.2017.10.126.

[39] Ali U, Rehman K, Alshomrani A S and Malik MY 2018 Thermal and Concentration Aspects in Carreau Viscosity Model Via Wedge, Case Studies in Thermal Engineering **12** 126-133 https://doi.org/10.1016/j.csite.2018.04.007.

[40] Goqo S P, Oloniiju S D, Mondal H, Sibanda P and Motsa S S, Entropy generation in MHD radiative viscous nanofluid flow over a porous wedge using the bivariate spectral quasi-linearization method, Case Studies in Thermal Engineering, https://doi.org/10.1016/j.csite.2018.10.005.

[41] Atif S M, Hussain S and Saghee M 2019 Heat and mass transfer analysis of time-dependent tangent hyperbolic nanofluid flow past a wedge. Physics Letters A, **11(25)** 1187-1198 doi:10.1016/j.physleta.2019.01.003.

[42] Kuo B L 2003 Application of the differential transformation method to the solutions of Falkner-Skan wedge flow, Acta Mech. **164** 161-174.

[43] Nadeem S, Ahmad S and Muhammad N 2018 Computational study of Falkner-Skan problem for a static and moving wedge. Sensors and Actuators B: Chemical, **263**, 69–76. doi:10.1016/j.snb.2018.02.039

[44] Reddy R C S and Reddy P S 2020 A comparative analysis of unsteady and steady Buongiorno's Williamson nanoliquid flow over a wedge with slip effects. Chinese Journal of Chemical Engineering. doi:10.1016/j.cjche.2020.04.016.

[45] Subbarayudu K,Suneetha S, Reddy P B A 2020 The assessment of time dependent flow of Williamson fluid with radiative blood flow against a wedge. Propulsion and Power Research. **9(1)**, 87-99. https://doi.org/10.1016/j.jppr.2019.07.001.

[46] Shahzad M, Ali M, Sultan F, Khan A W and Hussain Z 2020 Computational investigation of magneto-cross fluid flow with multiple slip along wedge and chemically reactive species. Results in Physics, **16**, 102972. doi:10.1016/j.rinp.2020.102972.

[47] Hamid A 2020 Existence of dual solutions for wedge flow of magneto-Williamson nanofluid: A revised model. Alexandria Engineering Journal **59 (3)** 1525–1537. doi:10.1016/j.aej.2020.04.001.

[48] Ali B, Hussain S, Nie Y, Rehman A and Khalid M 2020 Buoyancy Effetcs On FalknerSkan Flow of a Maxwell Nanofluid Fluid With Activation Energy past a wedge: Finite Element Approach, Chinese Journal of Physics **68** 368-380, doi: https://doi.org/10.1016/j.cjph.2020.09.026.